BSGF - Earth Sciences Bulletin 2024, 195, 14
© F. Demory *et al.*, Published by EDP Sciences 2024
https://doi.org/10.1051/bsgf/2024014

BSGF Earth Sciences Bulletin
Available online at:
www.bsgf.fr

Open Access

Dating the late Miocene marine sediments around the southern middle Durance valley (Provence, SE France): new evidences for a Tortonian age

François Demory[1,*], Doriane Delanghe[1], Régis Braucher[1], Pierre-Henri Blard[2], Alexis Nutz[1], Gilles Conesa[1], Gaëlle Ségué-Passama[1,3], Fabrice Hollender[4,5], Cédric Duvail[6], Anna Fioravanti[6], Laetitia Léanni[1], Aster Team[a,1] and Olivier Bellier[1,7]

[1] Aix Marseille Univ., CNRS, IRD, INRAE, College De France, CEREGE, Aix-en-Provence, France
[2] Centre de Recherches Pétrographiques et Géochimiques (CRPG), UMR 7358, CNRS, Université de Lorraine, Vandœuvre-lès-Nancy, France
[3] GeoSphere Austria, Department of Geophysics and Conrad Observatorium, Hohe Warte 38, 1190 Vienna, Austria
[4] French Alternative Energies and Atomic Energy Commission (CEA), DES, CEA Cadarache, Saint Paul, Lez Durance, France
[5] University Grenoble Alpes, University Savoie Mont Blanc, CNRS, IRD, University Gustave Eiffel, ISTerre, Grenoble, France
[6] Ginger CEBTP, division Géosciences, Jacou, France
[7] Aix Marseille Univ, CNRS, FR ECCOREV, Aix-en-Provence, France

Received: 23 August 2023 / Accepted: 5 June 2024 / Publishing online: 5 August 2024

Abstract – The present study aims dating the topmost 50 m of a 115 m-long core retrieved from a valley located in the Cadarache Area (Upper Provence, South East France). Based on burial dating by *in situ* produced cosmogenic nuclides (^{10}Be, ^{26}Al and ^{21}Ne), and paleomagnetic analyses, a Tortonian age was determined for the sedimentary succession exhibited in the core. In addition, thin sections, grain size analyses and quartz morphoscopy were used to characterize a shallow marine environment and to correlate the sediment core to the surrounding exposed sections. When comparing the studied sedimentary record to global sea level estimates, we establish that the local Tortonian transgression was not synchronous with the global scale sea level high-stand, but happened more likely later, during a global regressive trend. The timing of the Tortonian flooding in Upper Provence was therefore most probably driven by regional tectonic forcing.
Finally, the Tortonian shallow marine sediments are topped by lacustrine tight carbonates. These carbonates protect the marine sediments from the following major erosional events resulting from the Messinian sea level drop and from interglacial-glacial fluctuations that both yielded to the present-day valley topography.

Keywords: cosmogenic nuclides / paleomagnetism / dating / Miocene / marine sediments / vallée de la Durance / Tortonien / Provence

Résumé – Datation des sédiments marins du Miocène supérieur autour du sud de la vallée de la moyenne Durance (Provence, SE France) : nouvelles évidences pour un âge Tortonien. Cette étude propose de dater les 50 premiers mètres d'une carotte de 115 m prélevée dans une vallée dans le secteur de Cadarache (Haute Provence, sud-est de la France). La datation de l'enfouissement par les nucléides cosmogéniques produits *in situ* (^{10}Be, ^{26}Al et ^{21}Ne) et les analyses paléomagnétiques ont permis de déterminer un âge Tortonien pour la succession sédimentaire contenue dans la carotte. En outre, des lames minces, des analyses granulométriques et la morphoscopie des quartz ont été utilisées pour caractériser un environnement marin peu profond et pour établir une corrélation entre les sédiments de la carotte et les affleurements environnants. En comparant l'enregistrement sédimentaire étudié aux estimations du niveau de la mer à l'échelle mondiale, nous établissons que la transgression du Tortonien n'était localement pas synchrone de l'élévation du niveau de la mer à l'échelle mondiale, mais qu'elle s'est plutôt produite plus

*e-mail: demory@cerege.fr
[a] ASTER Team: Georges Aumaitre, Didier Bourlès, Karim Keddadouche.

tard, au cours d'une tendance régressive globale. Le moment de l'inondation au Tortonien en Haute Provence a donc très probablement été déterminé par des forçages tectoniques régionaux.
Enfin, les sédiments marins peu profonds du Tortonien sont surmontés de carbonates lacustres. Ces carbonates protègent les sédiments marins des événements postérieurs d'érosion majeur, résultant de la baisse du niveau de la mer au Messinien et des fluctuations interglaciaires qui ont toutes deux donné lieu à la topographie actuelle de la vallée.

Mots clés : nucléides cosmogéniques / paléomagnétisme / datation / Miocène / sédiments marins / Durance valley / Tortonian / Provence

1 Introduction

In the beginning of the seventies, the effects of the Mediterranean drought during the Messinian event have been observed on continental margins by the record of intense erosion creating deep canyons flooded by posterior transgression (Bache *et al.*, 2012 and references therein). Consequently, ancient Tertiary sedimentary succession chronologies in South-East France have to be revisited. Indeed, many geological maps are obsolete and do not consider this event in their interpretations. Messinian erosion and alpine tectonics left scarce and discontinuous outcrops of Miocene in Provence region (South East France). The last Miocene transgression occurring during the early Tortonian (Demarcq, 1984) is therefore poorly documented and weakly correlated. The Miocene marine sedimentary successions are generally dated with macrofossils – mostly molluscs – assemblages (*e.g.*, Demarcq, 1990) which are weak biostratigraphic markers. Chemostratigraphy based on $^{87}Sr/^{86}Sr$ was also applied to establish a chronology for successive transgressive sedimentation from Burdigalian to Serravallian (Besson *et al.*, 2005 and references therein). Finally, micropaleontology (nannofossils and foraminifera) together with paleomagnetism yielded Aquitanian-Burdigalian ages for marine sediments of southern Provence (Demory *et al.*, 2011).

In order to determine an accurate age for the last late Miocene transgression predating the Messinian event, we propose here a multidisciplinary approach to characterize and date the marine sedimentary rocks preserved in the Cadarache area. This later is located in a valley called "vallon de la bête" inherited from a graben that formed during the Oligocene extension. A Messinian canyon present in the vicinity of the valley strongly questioned the age of its sedimentary filling (Guyonnet Benaize, 2011). We date here the deposition age of cored sediments by measuring their contents in in situ produced cosmogenic nuclides with different half-lives (^{26}Al,^{10}Be) or stable (^{21}Ne) and by magnetostratigraphy.

2. Geological settings

Miocene in Provence area is characterized by successive marine transgressions responsible for a complex sedimentation in terms of geometry and facies due to a paleotopography inherited from the Pyrenean-Provencal orogenesis (Upper Cretaceous to Eocene) and the subsequent Oligocene extension. In addition, Provence region is affected by several sedimentary pulses and deformations linked to the alpine orogeny (Besson, 2005 and references therein). Finally, Miocene sediments had been affected by erosion, mainly due to the Messinian drought event (5.96–5.33 Ma; Krijgsman *et al.*, 1999). As a consequence of this complex geological history, Miocene sedimentary rocks in Provence and especially in the Cadarache area are often poorly exposed (Fig. 1A). Moreover, Miocene sediment successions outcropping or retrieved from cores need to be cautiously dated and correlated, which is a challenging task given the scarcity of suited fossils assemblages in these Miocene environments. Despite these difficulties, seven Miocene transgressive sequences have been recognized at regional scale (Fig. 1B). In this study, we analyzed the topmost 50 m of a 115 m-long sediment core (EOL 101) retrieved from the "Vallon de la Bête" area (Fig. 1C), *i.e.*, a small valley located within the CEA (Commissariat à l'Energie Atomique), as well as sediments exposed in the surroundings (B to E in Figs. 1C and 2). Both sedimentary successions have been previously attributed to late Miocene, but their exact ages of deposition remain poorly constrained (Guyonnet Benaize, 2011 and references therein).

3 Material and methods

3.1 Sedimentology

Grain-size distribution of the siliciclastic fraction of 74 samples from the core and from some selected outcrops inside the Vallon de la Bête area (Cascade, Bargette) and outside this area (Mirabeau, Saint Eucher) was determined with a Beckman Coulter LS 13 320 laser granulometer at CEREGE (Aix en Provence). The analytical procedure is described in *e.g.*, Ghilardi *et al.* (2014) and Sharifi *et al.* (2018). The particle size limits follow the recent classification of Blott and Pye (2012). The reproducibility of the analyses obtained using the BC LS 13 320 have been carefully evaluated (Lepage *et al.*, 2019).

Carbonate content was determined for the same levels with the automatic calcimeter Dream Electronique (*e.g.*, Martinez *et al.*, 2020) calibrated using a standard composed of >99% of $CaCO_3$. We analyzed several aliquots of 100 mg and 200 mg. Five replicates of 100 mg gave a reproducibility of 3% and 13 replicates of 200 mg samples yield a reproducibility of 0.1%. We then decided to analyze 200 mg samples. 3 replicates on a set of 9 samples are characterized by a 1 to 10% reproducibility at 2 sigmas.

The shape and the surface state of quartz grains were determined in 5 different sedimentary levels using a Leica M125 stereomicroscope. This brings information about the dynamic processes which had affected the sediments during their transportation in the watershed and/or in their environ-

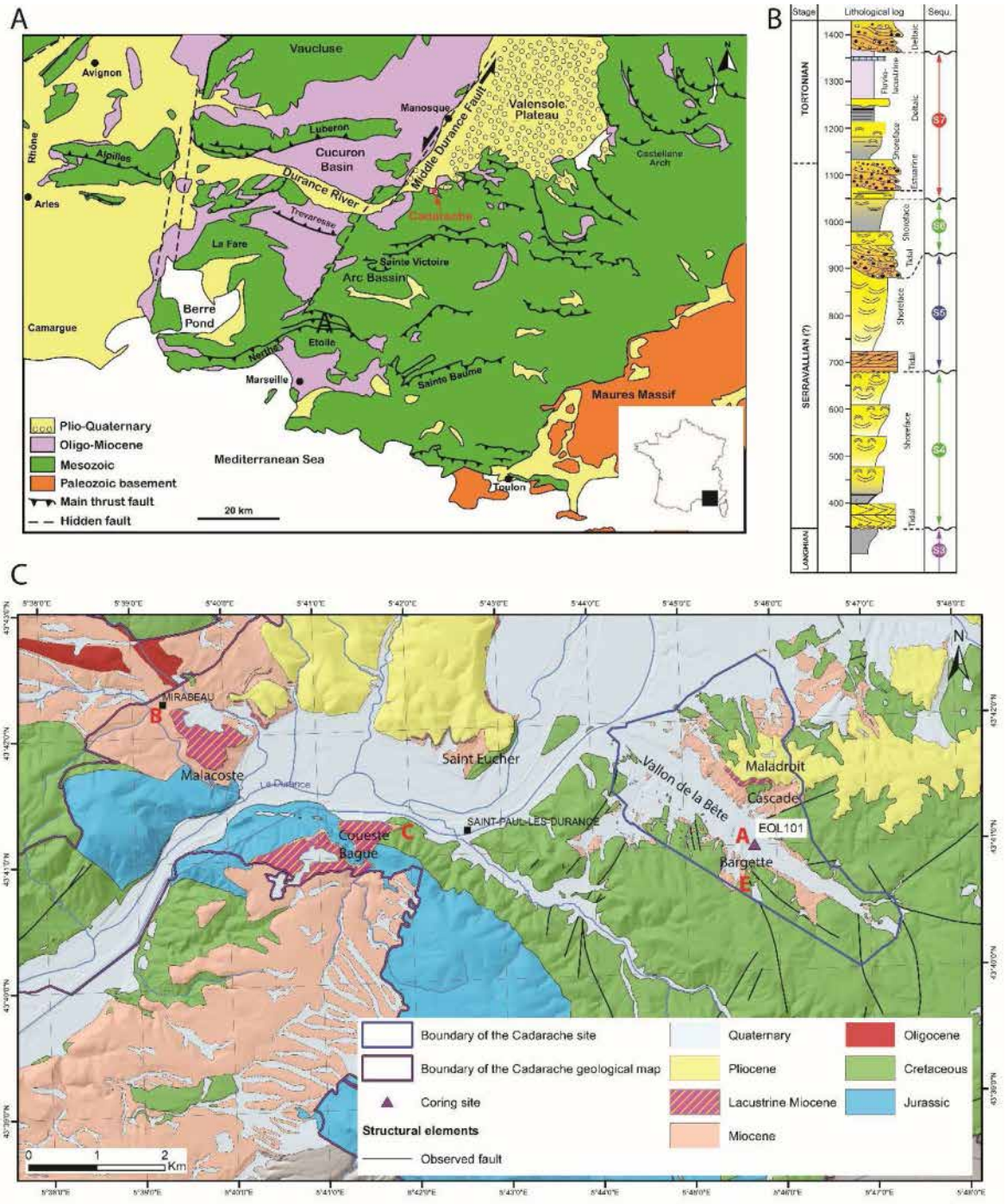

Fig. 1. A. Structural map of the Provence (modified after Demory *et al.*, 2010); B. Synthetic log of the upper part of the Miocene in Provence (modified after Besson *et al.*, 2005 and references therein). C. Geological map based on the geological map of Pertuis (Gouvernet *et al.*, 1970) in its southwest and northwest parts and revised for the rest of the map (Guyonnet-Benaize, 2011 and references therein), with location of core EOL101 (A) and keys outcrops (B to E).

ment of deposition. The sediment was prepared following a protocol established by Georges (2004), slightly modified by Kalinska and Nartiss (2014). After carbonates and organic matter removal and sieving into three granulometric classes (fine, medium to coarse grains), more than 1100 quartz in total were counted among other grains under a polarizing filter. Following Kalinska and Nartiss (2014), we defined 4 classes grouping the quartz grains according to both their rounding state and the frosting at their surfaces: NU (non-abraded shiny and frosted grains), EM/RM (partially rounded frosted grains), EM/EL (partially rounded shiny grains) and EL (well-rounded shiny grains). Indeed, most of the grains display shiny surfaces whatever their original surface state. However, some rounded or partially rounded frosted grains remain. We then propose to

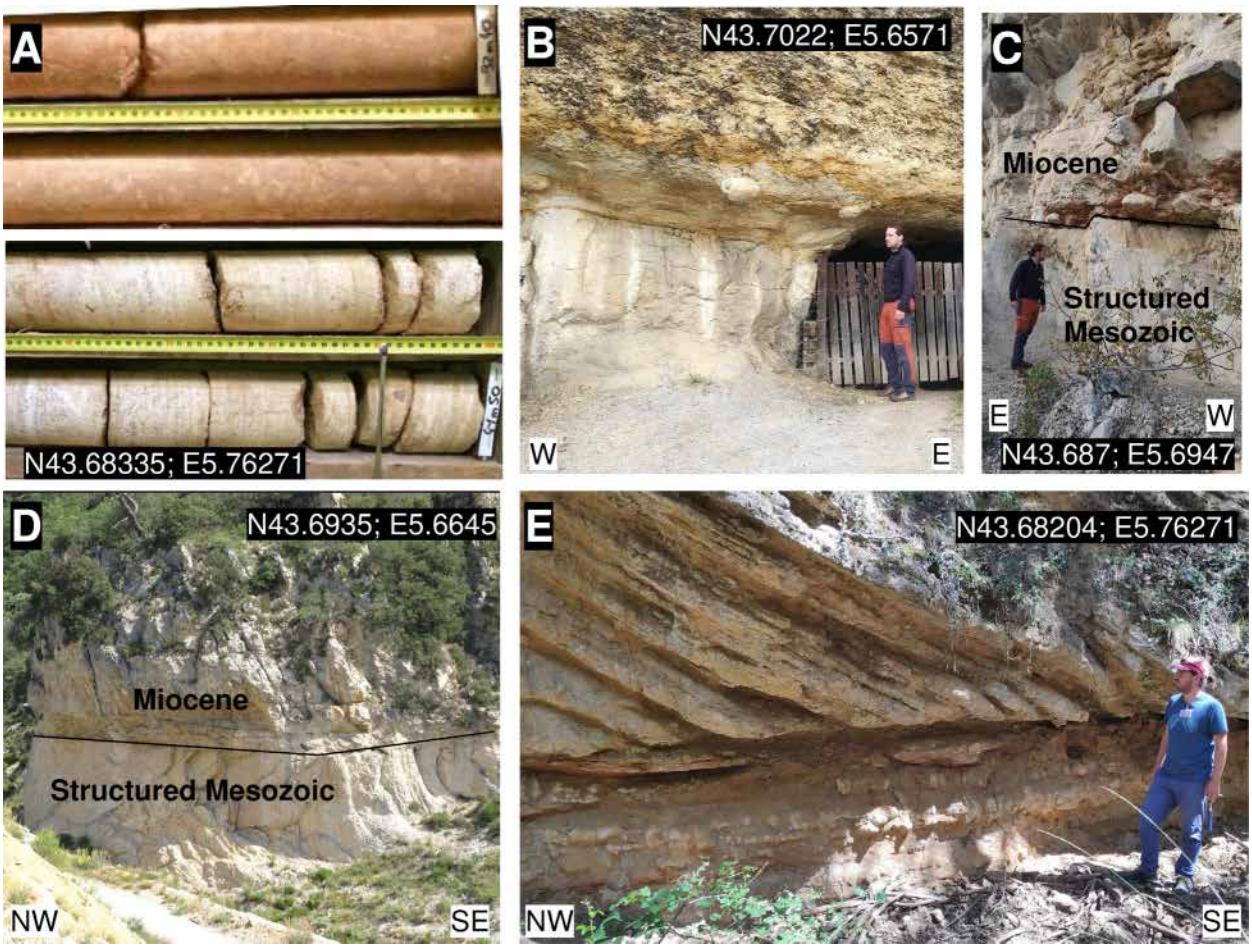

Fig. 2. Pictures of selected sections of core EOL 101 (A) and key outcrops: the Late Miocene marine sediments in Mirabeau area (B), transgressive surface on both side of the durance river (C and D) and a foresets sedimentary structure close to the core location (E).

combine here RM and EM/RM grains into the EM/RM class, while the non-abraded quartz are NU class. Most of the shiny quartz were either originally rounded frosted grains or partially rounded shiny grains.

To confirm the marine environment of the sedimentation, thin sections were prepared from samples of the two layers presenting the highest carbonate and bioclastic contents (depths 4 m and 42 m) and observed using an optical microscope under polarized light.

3.2 Magnetic susceptibility and paleomagnetism

In order to provide constraints on the paleoenvironmental conditions of the detrital inputs, low field magnetic susceptibility has been directly measured in contact with the sediment surface of the core using a SM30 susceptibilimeter (ZH Instruments). Eight cubic samples were measured in the paleomagnetic laboratory of the CEREGE using the MFK1 susceptibilimeter (AGICO) to calibrate *in situ* measurements and to determine specific (or massic) magnetic susceptibility. We considered a constant density after mass measurement of this panel of samples.

In order to determine geomagnetic polarities recorded in the sedimentary section and use them as an indirect dating tool, paleomagnetic investigations were conducted at the paleomagnetic laboratory of the CEREGE on 6 layers of core EOL 101. As the sediment core is highly porous and affected by late water circulations (Cartalade, 2002), we selected the most lithified layers in order to avoid total remagnetizations. Paleomagnetic investigations were done using the Superconducting Rock Magnetometer SRM760R (2G Enterprises), the Alternating Field (AF) system on-line and an ASC oven for the thermal demagnetization. After tests of thermal demagnetizations up to 300 °C and AF demagnetization of the Natural Remanent Magnetization (NRM) led on 8 samples respectively, stepwise thermal demagnetization of the NRM up to 600 °C and 700 °C (depending on the residual signal) was done on 24 samples retrieved from 6 layers in order to reach a satisfying repeatability of the results.

3.3 Cosmogenic nuclides

Cosmogenic nuclides with different half-lives (^{10}Be, 1.4 Ma and ^{26}Al, 0.7 Ma, and ^{21}Ne, stable) are here used to determine the burial age of sediments (*e.g.*, Sartégou *et al.*, 2018). While the couple ^{26}Al-^{10}Be permit to date deposition events between 0.5 and 5 Ma (*e.g.*, Granger and Muzikar, 2001), the couple

^{21}Ne-^{10}Be is better suited to date older sediments, from 5 Ma, and beyond 10 Ma (*e.g.*, Balco and Shuster, 2009).

3.3.1 Preparation of sample for ^{10}Be, ^{26}Al and ^{21}Ne

In this study, 6 samples were collected in EOL101 core and prepared for ^{10}Be ^{26}Al and ^{21}Ne analyses. The ^{26}Al and ^{10}Be preparation was performed at CEREGE (Aix-en-Provence, France). Extraction of ^{10}Be and ^{26}Al from the rock samples follows the chemical procedure of Brown *et al.* (1991) and Merchel and Herpers (1999). Samples were crushed and sieved to process the 250–1000 μm fraction. Quartz was concentrated by magnetic separation and selective dissolution in a 1/3 HCl − 2/3 H_2SiF_6 mixture. Atmospheric ^{10}Be was then eliminated by dissolving 30% in mass *via* three successive HF leaching processes. Pure quartz samples with a typical mass of ∼30 g were then spiked with 100 μL of a (3025±9)-ppm in-house ^{9}Be carrier (Merchel *et al.*, 2008) and totally dissolved in concentrated HF. Natural ^{27}Al concentrations in the dissolved samples were measured by inductively coupled plasma optical emission spectrometry (ICP-OES) on an ICAP6500 Thermo Scientific unit spectrometer.

Be and Al were extracted and purified using a succession of alkaline precipitation and separations on cationic and anionic exchange resins. BeO and Al_2O_3 were produced from hydroxides after oxidization performed at 700 °C for 1 h. Prior to AMS measurements, BeO and Al_2O_3 oxides were mixed with Nb conductive powder and Ag conductive powder, respectively, and then introduced in a copper cathode to be pressed.

3.3.2 Measurement of in situ cosmogenic ^{10}Be, ^{26}Al

The ^{10}Be/^{9}Be and ^{26}Al/^{27}Al ratios were measured at the French national AMS facility ASTER. The ^{10}Be/^{9}Be beryllium data were calibrated directly against the STD11 standard (Braucher *et al.*, 2015) with a ^{10}Be/^{9}Be ratio of $(1.191 \pm 0.013) \times 10^{-11}$, which is equivalent to the KNSTD07 standardization (Nishiizumi *et al.*, 2007). The measured ^{26}Al/^{27}Al ratios were calibrated against the ASTER in-house standard SM-Al-11, whose nominal value is ^{26}Al/^{27}Al = $(7.401 \pm 0.064) \times 10^{-12}$ (Merchel and Bremser, 2004). The used half-lives (^{10}Be: 1.387 ± 0.012 Ma (Chmeleff *et al.*, 2010; Korschinek *et al.*, 2010); ^{26}Al: 0.705 ± 0.024 Ma (Norris *et al.*, 1983) and the standardization method employed at ASTER (SM-Al-11/07KNSTD) imply that the ^{26}Al/^{10}Be spallation production ratio is ∼6.61 ± 0.52. The analytical uncertainties include the counting statistics, machine stability (∼0.5%; Arnold *et al.*, 2010 for ^{10}Be) and blank correction.

3.3.3 Measurement of in situ cosmogenic ^{21}Ne

Neon isotopic ratios and their concentrations in quartz were measured at the CRPG Nancy noble gas laboratory. Aliquots of quartz that were already purified by partial HF dissolution were processed for the neon analysis. Aliquots having a typical mass of ∼100 mg were wrapped in tin foils (melting point at 230 °C) and loaded in the carrousel of the full-metal induction furnace designed at CRPG (Zimmermann *et al.*, 2018). The furnace and the entire purification line were then baked at 150 °C overnight under high vacuum. Subsequently, the furnace crucible was degassed at >1500 °C under pumping to reduce the neon blanks.

Following conclusive validation tests, neon was extracted in two heating steps at 700 °C and 1400 °C for 20 min, for most of the samples. After each analysis, any remaining gas was pumped. Neon isotopes were corrected for hot furnace blanks and instrumental mass fractionations. Isobaric interference of $H_2{}^{18}O$ on ^{20}Ne was determined for each sample by measuring $H_2{}^{16}O$ and considering that the ($H_2{}^{16}O/H_2{}^{18}O$) ratio is 495 (Honda *et al.*, 2015). This ratio corresponds to a correction lower than 0.1%.

The neon extracted from these quartz samples is mainly a mixture of cosmogenic and atmospheric neon, which are in fluid inclusions and adsorbed at the grains surface (Niedermann, 2002). This atmospheric contribution was hence corrected using the following formula (Vermeesch *et al.*, 2012):

$$21\mathrm{Ne}_{\mathrm{cos}} = \mathrm{R_c} \times {}^{20}\mathrm{Ne_m} \times \frac{\mathrm{R_m} - \mathrm{R_a}}{\mathrm{R_c} - \mathrm{R_a}}, \quad (1)$$

where $^{21}\mathrm{Ne}_{\mathrm{cos}}$ is the cosmogenic ^{21}Ne concentration, $^{20}\mathrm{Ne}_{\mathrm{m}}$ (at.g^{-1}) is the amount of measured ^{20}Ne; $R_c = 0.8$ is the cosmogenic ^{21}Ne/^{20}Ne production ratio, R_m is the measured ^{21}Ne/^{20}Ne ratio; and $R_a = 0.002905$ is the atmospheric ^{21}Ne/^{20}Ne ratio (Honda *et al.*, 2015). We also corrected the $^{21}\mathrm{Ne}_{\mathrm{cos}}$ concentrations for the build-up of nucleogenic ^{21}Ne; for all samples, we assumed a nucleogenic production rate of 0.1 at.g^{-1}.yr^{-1} (Balco *et al.*, 2019; Sartégou *et al.*, 2020) and an age of 10 Ma for the samples cooling below the 100 °C isotherm (Schwartz *et al.*, 2017), ∼100 °C being the Ne closure temperature for such sub-millimetric quartz (Shuster and Farley, 2005). This corresponds to a total accumulation of nucleogenic ^{3}He of 10^6 at.g^{-1}, between 5 and 11% of the measured $^{21}\mathrm{Ne}_{\mathrm{cos}}$s concentrations. For each sample, we measured two neon aliquots. All of them agree within uncertainties and we thus computed weighed mean of cosmogenic ^{21}Ne concentrations before calculating the burial ages (Supp. Table Cosmo).

To calculate the burial ages, we considered the elevation of the watershed during the paleo-exposure of the detrital material, before its instantaneous burial under sea level. For this, we applied the following equations (Blard *et al.*, 2019a), using the Matlab Monte Carlo codes of (Blard *et al.*, 2019b) that permit to compute calculate burial ages and the associated uncertainties:

$$\frac{P_1}{N_1} e^{-\lambda_1 t_{burial}} - \frac{P_2}{N_2} e^{-\lambda_2 t_{burial}} = \frac{\lambda_1 - \lambda_2}{f}, \quad (2)$$

where f is the spatial scaling factor, P_1 and P_2 (at.g^{-1}.yr^{-1}) are the respective sea level high latitude production rates of nuclides 1 and 2, whose respective concentrations are N_1 and N_2 (at.g^{-1}) and radioactive decay constant λ_1 and λ_2. Here we used a SLHL ^{10}Be production rate of 4.02±0.32 at/g (Borchers *et al.*, 2016) with an ^{26}Al/^{10}Be spallation ratio of 6.61±0.5 (Rixhon *et al.*, 2011) and a ^{21}Ne/^{10}Be spallation ratio of 4.1 ±0.4 (Balco and Shuster, 2009). We report the burial ages considering a moderate watershed paleo-elevation of 500 m. This value has been estimated using the present-day average elevation of the Lower Provence (441 m, according to

de Martonne, 1941) that may be similar to the late Miocene topography close to the shore and that includes the average altitude of several watersheds. Computed ages assuming higher elevations are also presented in Supp. Table Cosmo.

4 Results

4.1 Sedimentology

Core EOL 101 is mainly composed of carbonate more or less cemented sandstones (Fig. 2A) with some layers enriched in bioclasts overlying breccia observed at the bottom of the core. This monogenetic breccia locally generated from mesosoic basement has not been here studied. The topmost 4 meters of the sedimentary sequence is altered (Fig. 3A). These sandstones are similar to Late Miocene sediments described around the Mirabeau area (Fig. 2B). They overlay an unconformity observed on both sides of Durance river (Figs. 2C and Figs 2D) and interpreted as an abrasive marine surface due to the transgression onto Mesozoic substratum. A large outcrop of carbonate sandstones is observed close to the core site, at slightly higher altitude. This outcrop shows plurimetric and dipping landward foresets (Fig. 2E). They are interpreted as washover fans internal structures (Hails, 1984). The geological map shows that the late Miocene marine sediments around Cadarache site are overlain by lacustrine limestones (Fig. 1C), that protected them from Messinian erosion (Guyonnet Benaize, 2011).

Carbonate content ranges from 5% to 74%, with an average around 20-30% (Fig. 3A). The lowest carbonate content values are characteristics of poorly cemented sandstones, located around a depth of 12 m, while $CaCO_3$ concentrations are the highest between 28 and 43 m, where the sandstones are highly cemented, with bioclasts-rich layers.

Despite a lower resolution, some high values of $CaCO_3$ corresponds to the lowest values of magnetic susceptibility (Fig. 3A). This later ranges from negative values in carbonate-rich layers up to almost 60 10^{-8} m^3kg^{-1} in sediments enriched in paramagnetic clays and ferromagnetic particles (most probably hematite according to the reddish color of the sediment).

Grain sizes below 7 m depth are mainly medium sands with a principal mode ranging between 170 and 223 μm. The two other modes dominating the signal are at ~ 35 and 16 μm. Some levels with coarser grains are observed at different depths, notably in bioclastic rich layers, between 28 and 43 m, where the mode may reach 1 mm locally.

Figure 3B displays grain-size distributions from core samples and from surrounding outcrops (Fig. 1C). Cored and outcrops sediments display similar granulometric distributions. This argues that both sediments shared similar transportation dynamics.

Quartz morphoscopy shows that more than 70% of the observed grains display shiny surfaces, with different rounding and frosting degrees. The other clasts are either non-abraded or partially frosted grains. Oxides are visible on the surface of all grains.

The results displayed in Figure 4A show a clear dominance of partially rounded shiny (EM/EL) of medium size (around 200 μm) sand grains (10 to 40% of the total grains). Their significant proportions are found whatever the size classes and are in the same order of magnitude in the samples. The constant grain-sizes mode around 200 μm all along the core and the rounded-shiny surface state of the quartz grains argue for a water-driven media transport and relative rapid deposition of the sands with a remobilization of previous sands including grains of aeolian origin.

Thin section at depth 42 m (Fig. 4B up and middle) shows a poorly compacted, well sorted and with a bimodal classification facies. It is characterized by millimetric laminae, alternating with coarse bioclastic and fine quartz-rich sandstones.

Coarse sandstones are composed of abundant bioclasts and frequent blunt to very blunt lithoclasts displaying a fine micrite coating. The elongated elements are imbricated. Bioclasts are constituted of molluscs (bivalves or gastropods), very rare fragments of pectinids, ostreids, gastropods, scaphopods, echinoids, cirripeds, gracile bryozoans and small hyaline benthic foraminifera. Lithoclasts are either quartz grains from far distance origin, or carbonates (fractured mudstones and fine micropelloidal grainstones with rare milioles and echinoids) from nearby Mesozoic rocks. Some glauconite grains are also observed.

The facies of the thin section prepared from layer 4 m (Fig. 4B down) is a well sorted and poorly compacted fine to medium grain size sandstone. The mixed detrital fraction is composed of dominant rounded quartz and carbonate fragments (mudstones or, in very rare cases, echinoid wackestones). The very rare bioclasts are debris of echinoids, possible cirripedes and red algae, planktonic foraminifera with globular test filled by phosphate and small hyaline benthic foraminifera. A tiling phenomenon of the most elongated elements is also observed, as well as a thin isopaquous border of micritic cement surrounding the grains.

The facies observed at 42 m depth is characteristic of a coastal marine environment. Sand grains probably spent a long time on the sea bottom, where they were probably remobilized by the swell and the littoral drift. The facies observed at 4 m depth was probably deposited in a similar environment, as supported by few marine bioclasts, an early marine cementation, well sorted clasts with a discrete imbrication, the absence of a micritic matrix.

4.2 Paleomagnetism

The Natural Remanent Magnetization of the selected samples shown in Figure 5 ranges from 8 10^{-5} Am^{-1} to 6.86 10^{-3} Am^{-1}, that is much above the sensitivity of the magnetometer (~2 10^{-6} Am^{-1}, corresponding to a magnetic moment of 2 10^{-11} Am^2 for a standard volume of 10 cm^3). Only thermal demagnetization protocol was able to produce interpretable and reproducible results since hematite, resisting to the alternating field demagnetization, is one of the main carriers of the remanence according to the remaining remanence signal above 585 °C (Curie temperature of magnetite). Only paleomagnetic inclinations have been considered for interpretation since the core sections are not oriented in declination. All thermal demagnetization patterns (Fig. 5) show either the record of a clear stable negative inclination (*e.g.*, at depths 4.4 m and 34.3 m) or negative inclinations more or less largely overprinted by positive

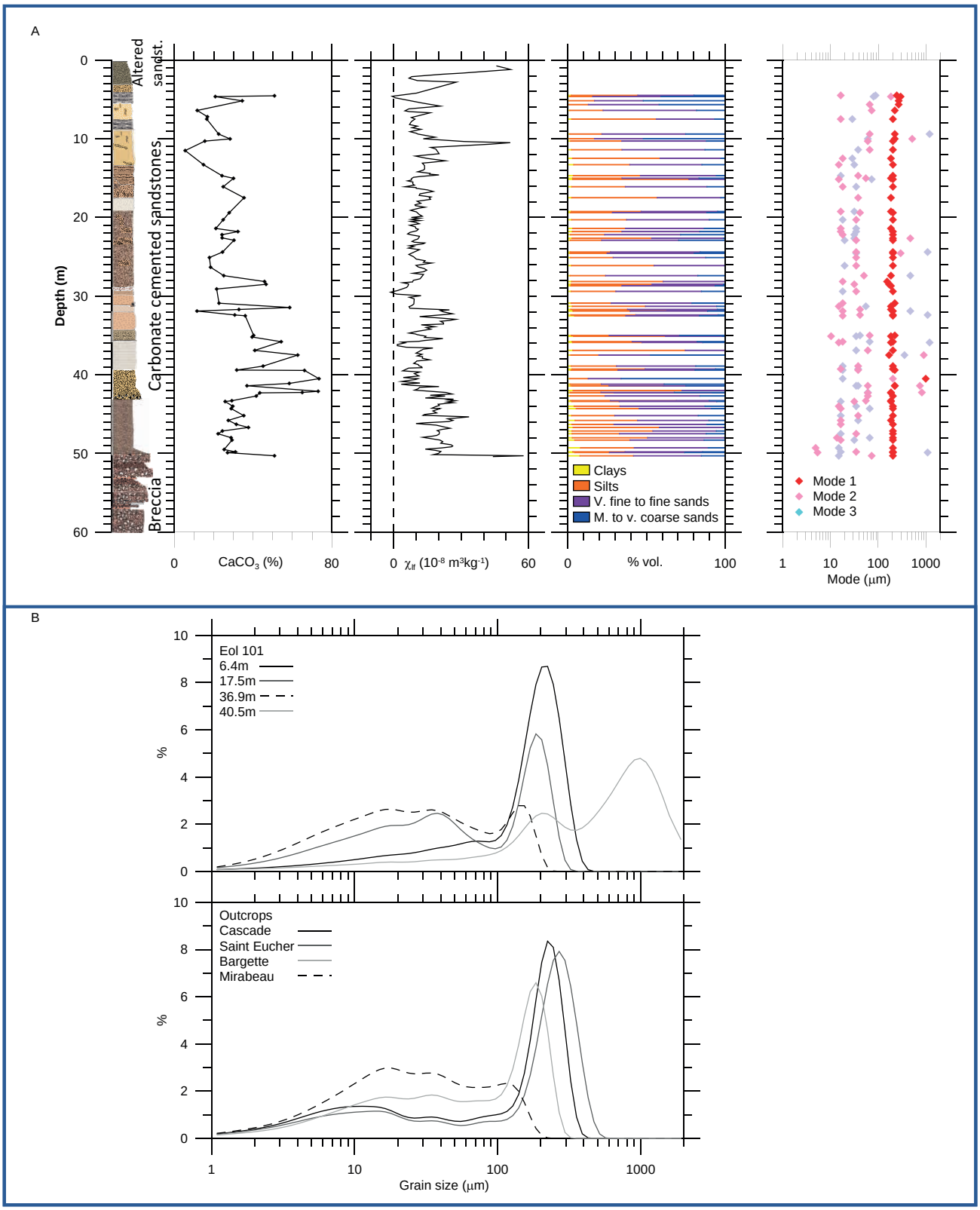

Fig. 3. A. Log of the core EOL101 with carbonate content, massic magnetic susceptibility and grain size textures and the main modes. B. Grain size distribution of samples retrieved from core EOL101 and surrounding outcrops (see Fig. 1C).

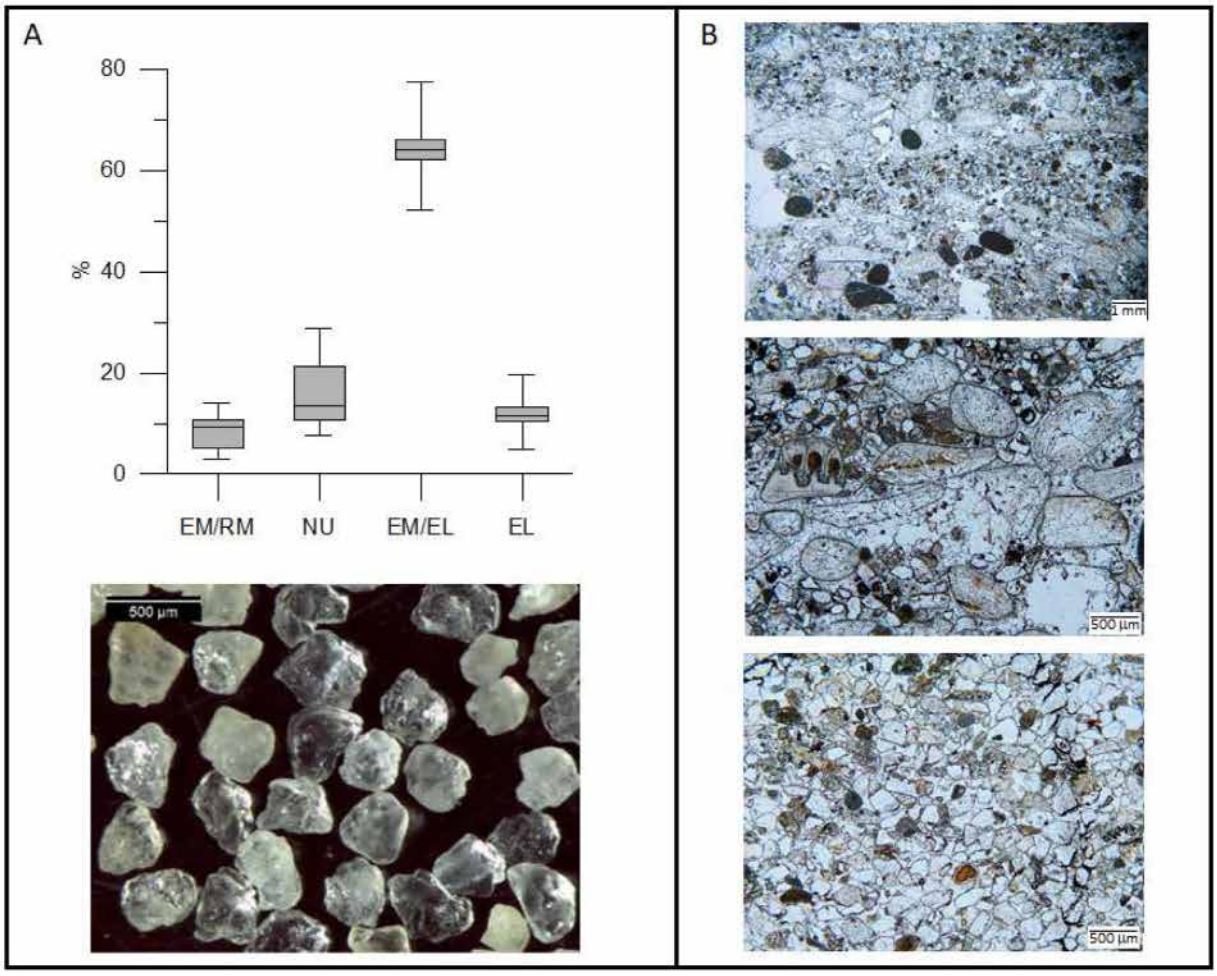

Fig. 4. A. Bar chart showing the proportion of the different grain surfaces after morphoscopic study led on 5 selected samples and a picture showing the most common quartz grain surfaces. B. Thin section pictures of samples collected from 2 carbonates-rich layers at 42 m-depth (picture on top and its close up in the middle) and at 4 m-depth (picture on the bottom).

inclinations displaying great circle patterns on the stereographic projections (*e.g.*, at depths 8.7 m, 18.1 m, 42.2 m and 47.5 m). Positive inclination overprints indicate a secondary record of the normal geomagnetic polarity of Brunhes linked to recent fluid circulations (Cartalade, 2002). Negative inclinations are attributed to the primary record (*i.e.*, the first locking after sedimentation) of a reverse geomagnetic polarity.

4.3 Burial ages from cosmogenic nuclides couples

Measured cosmogenic nuclides concentrations and burial ages are presented in the Supp. Table Cosmo. Old burial ages (>5 Ma), together with high natural ^{27}Al content did not favor high AMS ^{26}Al/^{27}Al ratios. Indeed, all measured ratios were on the order of 10^{-15} or lower (for two samples, CD42 and 46, no ^{26}Al atoms were detected). Hence, the burial ages are beyond the maximum range of the ^{26}Al/^{10}Be method (>5 Ma). This is confirmed by ^{10}Be/^{21}Ne burial ages that are much older than the ^{26}Al/^{10}Be ages: the 5 samples analyzed between 15 and 46 m yield ^{10}Be/^{21}Ne ages ranging from 9.34 ± 1.0 to 10.50 ± 0.60 Ma (Fig. 6). Since the sedimentological observations did not identify any sedimentation gap, we consider that the 5 dating points indicate a rapid deposition of the sandstone located between 50 and 5 m depth, that occurred between 10 and 9 Ma, in less than 1 Ma. Assuming that these 5 samples have undistinguishable deposition age, we produced a kernel density estimate to determine an average age of 9.75 ± 0.55 Ma representative of the deposition age of the sedimentary section between 46 and 15 m. A sixth sample, collected at shallower depth (4 m) has a ^{26}Al/^{10}Be burial age of 0.39 Ma, most probably due to a recent re-exposure.

5 Discussion

5.1 Dating implications

5.1.1 Origin of the Tortonian transgression: Global eustatic event *vs* tectonics

The 5 ^{10}Be/^{21}Ne burial ages determined from the well buried sediments between 15 and 46 m indicate that this sedimentary section was deposited during the Tortonian (Fig. 6). This dataset indicates a sedimentation rate of ~30 m/Ma between ~10.3 Ma and ~ 9.2 Ma. This sedimentation rate in a shallow sedimentary environment is

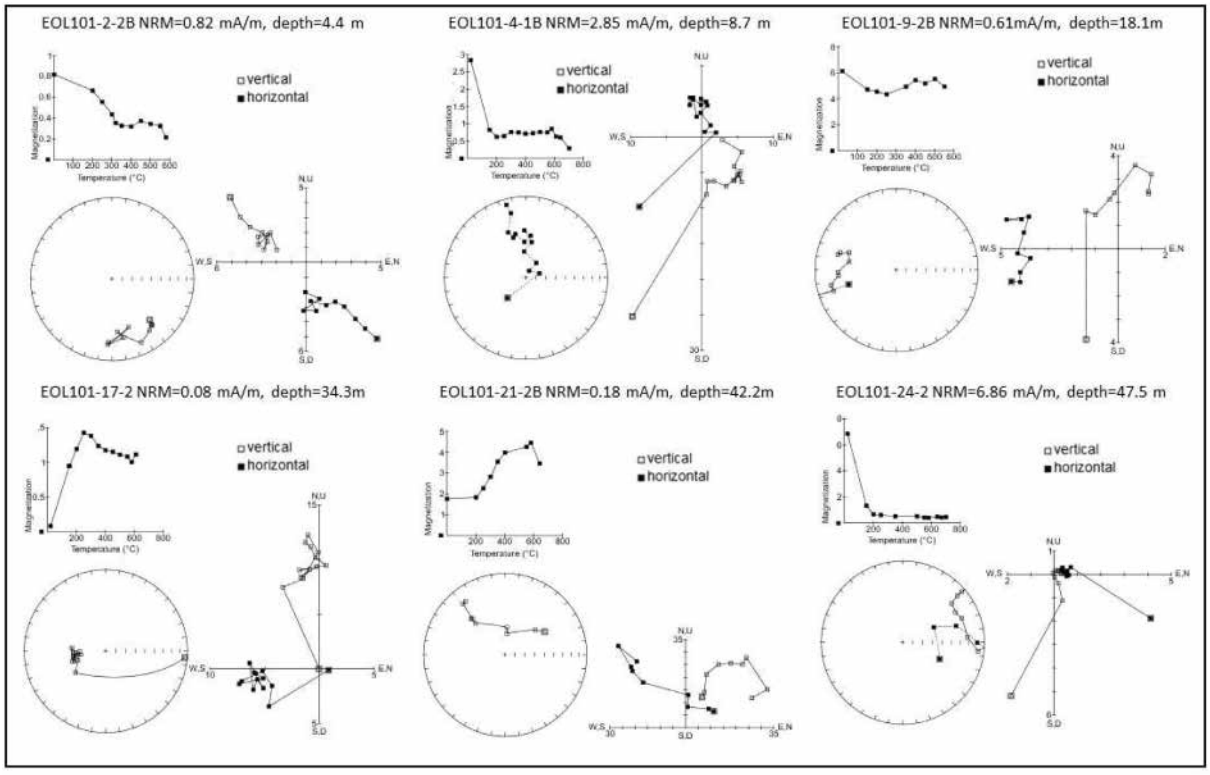

Fig. 5. paleomagnetic results of selected samples collected from 6 layers (demagnetization curve, stereographic and orthogonal projections): All samples show the record of a stable reverse polarity of the geomagnetic field more or less overprinted by a normal polarity component.

compatible with subsidence rates estimated on a modern continental margin (*e.g.*, ~ 56 m/Ma in the shallow part of Gulf of Lion, Rabineau *et al.*, 2014). The time interval of sedimentation is also compatible with the reverse polarities determined in the present study, since the reference polarity scale displays two long lasting reverse polarity periods between 9.105 and 9.311 Ma (C4Ar.1r) and between 9.426 and 9.647 Ma (C4Ar.1r). The normal polarity documented between 9.3 and 9.4 Ma can be missing due to the resolution of the paleomagnetic study. Hence, the combination of the $^{10}Be/^{21}Ne$ dating with the paleomagnetic data point toward a robust estimate of 9.10-9.65 Ma for the sedimentary section between 46 and 15 m. This age is younger than those presented in previous studies, in which the last Tortonian transgression was tuned to the early Tortonian high stand depicted in global marine records on the base of sequence stratigraphy (Demarcq, 1984; Besson, 2005). According to the global sea level reconstruction (Miller *et al.*, 2020) and the transgression/regression megacycles established in Hilgen *et al.* 2012, the transgressive shallow marine sediments of core EOL 101 were most probably deposited during a global regression during the 9.10–9.65 Ma interval. Although our age estimate is affected by uncertainties, the maximum global transgression level dated at 10.8 Ma happens during a normal polarity chron that is not compatible with the reverse polarities recorded in our sedimentary sequence. Hence, the accommodation space needed here for a sedimentation at 30 m/Ma rate is more likely due to regional tectonic subsidence than a global transgression phase. Apart from sediment load and regional thermal subsidence, vertical movements can also be due to tectonics that may result from multiple mechanisms. First, the foreland basin, in which the present study is located, is affected by successive tilting. One of these tilting is quantified in the studied area with the slight dipping (~1.15°) at kilometer scale of the (horizontally deposited) lacustrine carbonates. This dipping toward SW is due to the uplift of Alpine front located in the NE of the Provence (Castellane Arch, Fig. 1A). Second, NNE-SSW crustal transform faults movements that opened large pull apart basins (Bestani, 2015 and references therein) are also able to produce accommodation. Finally, gravity tectonics through mass salt redistribution due to Alpine induced topography changing (Rangin *et al.*, 2010) may be also involved in the accommodation.

5.1.2 Post Miocene history of the valley

The shallower sediments (at 4 m-depth) of the core are also characterized by a negative paleomagnetic inclinations (Fig. 5) recording a geomagnetic reverse polarity (Fig. 6) at least older than 780 ka, but most probably of the same age than the other reverse polarities revealed by the core. The same shallower sediments are also characterized by a burial age of 0.32 Ma that is much younger that the underlying sediments (from 10 to 48 m) and incompatible with the record of a reverse polarity. Therefore, it turns out that the sediments on top of core EOL101 probably deposited in the same sedimentary event than the underlying sediments. The $^{26}Al/^{10}Be$ ages of these shallow sediments have probably been rejuvenated due to their high position in the sedimentary column *i.e.*, close to the surface, at a depth easily reachable by cosmogenic particle able

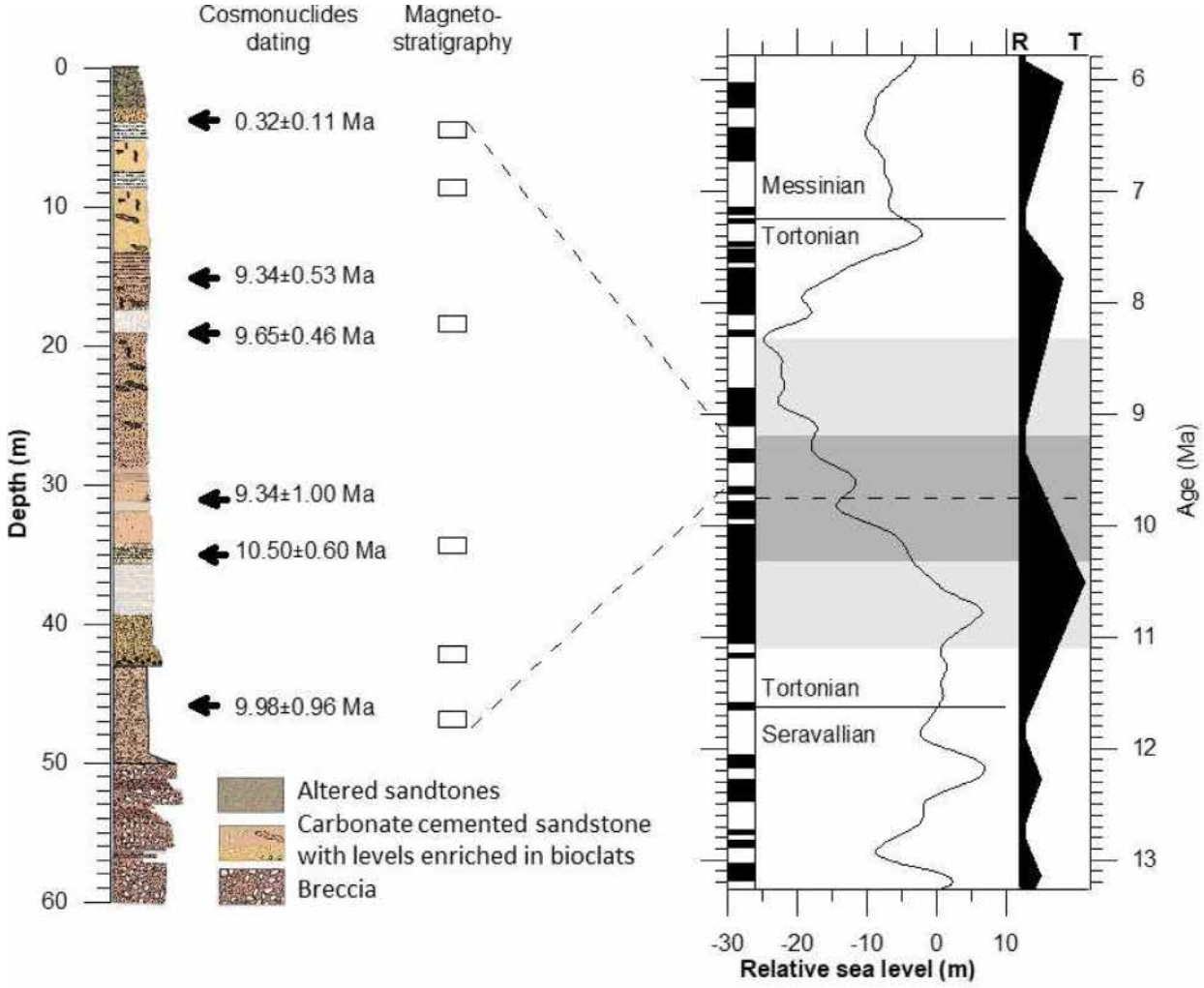

Fig. 6. Log of core EOL101 with cosmonuclides dates and paleomagnetic data compared to the relative sea level at global scale (Miller *et al.*, 2020) and to the regression-transgression megacycles (Hilgen *et al.*, 2012) and the reference geomagnetic scale (Ogg, 2012). The light grey interval in this figure corresponds to the Min-Max error bars of cosmonuclides dating and the gray interval corresponds to the confidence level determined from kernel statistics.

to produce cosmogenic nuclides. The present-day depth of the re-exposed sample in the core is probably due to erosion of the sediments filling the "vallon de la Bête" valley, since some Late Miocene sediments are preserved at higher altitude all around the coring site (Figs. 1C and Figs 2E). We attribute the initiation of this erosional event at the Messinian drought crisis, while erosion continued during the glacial/interglacial periods of the Quaternary.

5.2 Sedimentological correlation

The burial age and the shallow marine character of the sandstones of core EOL 101 being established, we tried to correlate these sandstones to the most continuous sedimentary succession exposed nearby – in the Malacoste-Mirabeau area – *i.e.*, ~8 km far to the west of the core EOL 101 location (Fig. 1C). Above the transgression observed in Malacoste area (Fig. 2D), the sedimentary succession attributed to upper Miocene is composed of a thick deposit of calcarenite with gravels and/or bioclastics layers intercalated, some layers display also oblique laminations. This calcarenite is supposed to have been deposited in an upper shoreface environment. The overlying sediments are composed of sandstones with few layers enriched in bioclasts, probably deposited in a shoreface environment. On the top of the sandstones, a thick calcarenite facies rich in bioclasts and obliques is attributed to an upper shoreface environment. The transition between lower and upper shoreface sedimentation can be observed in Figure 2B. The topmost part of the sequence is characterized by a lacustrine limestone. At regional scale, this sedimentary sequence is attributed to sequence 7 (Fig. 1B, Besson, 2005 and references therein), deposited during the last Miocene transgression. The lower shoreface facies of sandstones are very similar to the sandstones of Core EOL 101, with an equivalent thickness. In addition, the upper calcarenites of Malacoste-Mirabeau area (Fig. 6 left) could be correlated with nearshore sediments (*i.e.*, washover fan) described close to the core EOL101 location in Bargette area (Fig. 2E). The Lacustrine facies of the Malacoste-Mirabeau sequence is also

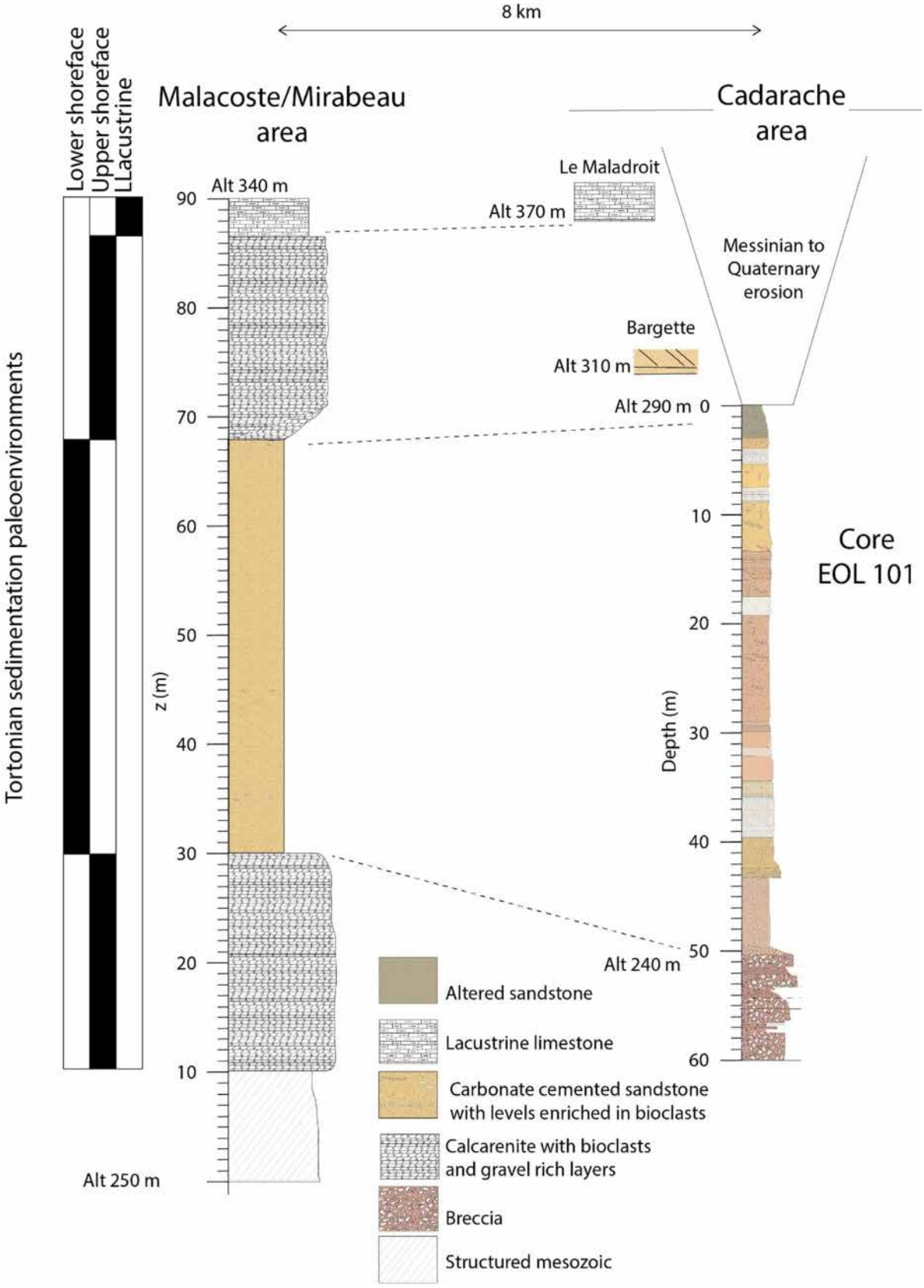

Fig. 7. Log and paleo-environmental reconstitution of the late Miocene sedimentary succession in the Mirabeau-Malacoste area correlated with the sedimentary sequence of core EOL101, some altitudes and some outcrops of "Vallon de la Bête" valley are also displayed. Supp. Table Cosmo: Be-Ne ages, ^{10}Be and ^{26}Al data and ^{21}Ne data.

observed on the northern flank of the "vallon de la Bête" valley (Maladroit in Fig. 1C). All correlations proposed between the sedimentary succession filling the "vallon de la Bête" valley (Fig. 7 right) and the sedimentary succession of the Malacoste-Mirabeau area (Fig. 7 left) are compatible in elevation. This compatibility has been tested in a previous study integrating a 3 D model, considering possible vertical movements after sedimentation due to tectonics (Guyonnet-Benaize, 2011). In addition to the regional correlation, our model also implies that the upper part of the Tortonian sedimentation is missing in the core EOL101 due to successive erosion processes happening after the last Miocene transgression (Fig. 7 right) and responsible for the present-day topography of the "vallon de la Bête" valley.

6 Conclusion

The present study proposes absolute ages for core EOL 101 retrieved from the "Vallon de la Bête" valley in which most of the infrastructures of CEA Cadarache site are located. Sedimentology and geochronological data (cosmogenic nuclides burial dating by ^{10}Be/^{26}Al/^{21}Ne and paleomagnetism) reveals that the marine sediments observed throughout the 50 m-long core have a Tortonian age, with a best age estimate ranging between 9.10 and 9.65 Ma. Comparing the facies, the relative thicknesses and altitudes with surrounding outcrops, lateral correlations indicate that the upper part of the Cadarache log belongs to the last sedimentary sequence before the Messinian drought event, and corresponds to the regional sequence 7. The dating shows that the sedimentation happens during a period of regression at global scale. The accommodation changes needed to develop the sedimentary sequence are most probably due to local subsidence tectonics. The dating of the shallowest sediment shows that the sediments suffered a post Miocene re-exposure due to erosion of the valley ranging from the Messinian drought event to the glacial-interglacial fluctuations of the Quaternary.

Acknowledgments

This study was conducted in the frame of the Cashima Research Project (CEA). Frédéric Magnien (IMBE) and Julien Longerey (CEREGE) are thanked for fruitful discussions and technical support respectively. Finally, two reviewers by their relevant comments helped improving the quality of the manuscript.

References

Arnold M, Merchel S, Bourles DL, *et al.* 2010. The French accelerator mass spectrometry facility ASTER: improved performance and developments. *Nucl Instrum Methods Phys Res B* 268: 1954–1959.

Bache F, Popescu SM, Rabineau M, *et al.* 2012. A two-step process for the reflooding of the Mediterranean after the Messinian Salinity Crisis. *Basin Res* 24: 125–153. https://doi.org/10.1111/j.1365-2117. 2011.00521.x

Balco G, Blard P-H., Shuster DL, Stone JOH, Zimmermann L. 2019. Cosmogenic and nucleogenic 21Ne in quartz in a 28-meter sandstone core from the McMurdo Dry Valleys, Antarctica. *Quat Geochronol* 52: 63–76. https://doi.org/10.1016/j.quageo.2019.02.006

Balco G, Shuster DL. 2009. Production rate of cosmogenic 21Ne in quartz estimated from ^{10}Be, ^{26}Al, and ^{21}Ne concentrations in slowly eroding Antarctic bedrock surfaces. *Earth Planet Sci Lett* 281: 48–58.

Besson D. 2005. Architecture du bassin rhodano-provençal miocène (Alpes, SE France). Relations entre déformation, physiographie et sédimentation dans un bassin molassique d'avant-pays (These de doctorat). Paris: ENMP.

Besson D, Parize O, Rubino JL, *et al.* 2005. Un réseau fluviatile d'âge burdigalien terminal dans le sud-est de la France : remplissage, extension, âge, implications. *C. R. Geosci* 337: 1045–1054.

Bestani L. 2015. Géométrie et cinématique de l'avant-pays provençal: modélisation par coupes équilibrées dans une zone à tectonique polyphasée (thesis). http://www.theses.fr Aix-Marseille.

Blard P-H., Lupker M, Rousseau M. 2019. Paired-cosmogenic nuclide paleoaltimetry. *Earth Planet Sci Lett* 515: 271–282. https://doi.org/10.1016/j.epsl.2019.03.005

Blard P-H., Lupker M, Rousseau M, Tesson J. 2019. Two MATLAB programs for computing paleo-elevations and burial ages from paired-cosmogenic nuclides. *MethodsX* 6: 1547–1556. https://doi.org/10.1016/j.mex.2019.05.017

Blott SJ, Pye K. 2012. Particle size scales and classification of sediment types based on particle size distributions: review and recommended procedures. *Sedimentology* 59: 2071–2096. https://doi.org/10.1111/j. 1365-3091. 2012.01335.x

Borchers B, Marrero S, Balco G, *et al.* 2016. Geological calibration of spallation production rates in the CRONUS-Earth project. *Quat Geochronol* 31: 188–198.

Braucher R, Guillou V, Bourlès DL, *et al.* 2015. Preparation of ASTER in-house10Be/9Be standard solutions. *Nucl Instrum Methods Phys Res B* 361: 335–340.

Brown ET, Edmond JM, Raisbeck GM, Yiou F, Kurz MD, Brook EJ. 1991. Examination of surface exposure ages of Antarctic moraines using in situ produced ^{10}Be and ^{26}Al: Geochim. *Cosmochim Acta* 55: 2269–2283.

Cartalade A. 2002. Modélisation des ecoulements dans les aquiferes fractures, developpement d'un modele multi-continua (problemes direct et inverse) et application au site du CEA /Cadarache. Hydrologie: Université Montpellier II.

Chmeleff J, von Blanckenburg F, Kossert K, Jakob J. 2010. Determination of the ^{10}Be half-life by multicollector ICP-MS and liquid scintillation counting. *Nucl Instrum Methods Phys Res B* 268: 192–199.

Demarcq G. 1984. Paléogéographie du Miocène. In: G. Demarcq, J. Perriaux *et al.* (coord.), *Synthèse géologique du Sud-Est de la France : Stratigraphie et paléogéographie*, Néogène in S. Debrand-Passard *et al.*, , Mém. BRGM, Orléans, 125, p. 503–506.

Demarcq G. 1990. Pectinidés néogènes: proposition d'échelle biostratigraphique pour la Méditerranée. *Geobios* 23: 149–159. https://doi.org/10.1016/S0016-6995(06) 80047-1

de Martonne E. 1941. L'altitude moyenne de la France et de ses grandes régions naturelles. *Bull Assoc Géogr Fr* 18: 2–4. https://doi.org/10.3406/bagf.1941.7093

Demory F, Arfib B, Lamarche J. 2010. La basse provence calcaire. In: P. Audra, A.F. de K. (Eds.), *Grottes et Karsts de France, Karstologia Mémoires* 19, pp. 236–237.

Demory F, Conesa G, Oudet J, *et al.* 2011. Magnetostratigraphy and paleoenvironments in shallow-water carbonates: the Oligocene-Miocene sediments of the northern margin of the Liguro-Provençal basin (West Marseille, southeastern France). *Bull Soc Géol Fr* 182: 37–55. https://doi.org/10.2113/gssgfbull.182.1.37

Georges K. 2004. Méthode de traitement statistique appliquée à l'exoscopie des quartz: environnements fluviaux et littoraux de Provence (Thèse de doctorat). Aix-Marseille 1.

Ghilardi M., Psomiadis D., Pavlopoulos K., Müller-Celka S., Fachard S., Theurillat T., Verdan S., Knodell A., Theodoropoulou T., Bicket A., Bonneau A., Delanghe- Sabatier D., 2014. Mid- to Late Holocene shoreline reconstruction and human occupation in Ancient Eretria (South Central Euboea, Greece). Geomorphology, 208, 225-237. http://dx.doi.org/10.1016/j.geomorph.2013.12.006

Gouvernet C, Rouire J, Rousset C. 1970. Pertuis. Notice de la carte géologique du BRGM à 1/50000,n°99

Granger DE, Muzikar PF. 2001. Dating sediment burial with in situ-produced cosmogenic nuclides: theory, techniques, and limitations. *Earth Planet Sci Lett* 188: 269–281. https://doi.org/10.1016/S0012-821X(01) 00309-0

Guyonnet-Benaize C. 2011. Modélisation 3D multi-échelle des structures géologiques de la région de la faille de la moyenne Durance (SE France) (These de doctorat). Aix-Marseille 1.

Hails JR. 1984. Washover and washover fan. In: M. Schwartz (Ed.), *Beaches and Coastal Geology*, *Encyclopedia of Earth Sciences Series*. New York, NY: Springer US, pp. 851–851. https://doi. org/10. 1007/0-387-30843-1_481

Hilgen FJ, Lourens LJ, Van Dam JA, *et al.* 2012. Chapter 29 – the Neogene period. In: F.M. Gradstein, J.G. Ogg, M.D. Schmitz, G.M. Ogg (Eds.),*The Geologic Time Scale. Boston: Elsevier*, pp. 923–978. https://doi. org/10. 1016/B978-0-444- 59425–9. 00029-9

Honda M, Zhang X, Phillips D, Hamilton D, Deerberg M, Schwieters JB. 2015. Redetermination of the ^{21}Ne relative abundance of the atmosphere, using a high resolution, multi-collector noble gas mass spectrometer (HELIX-MC Plus). *Int J Mass Spectrom* 387: 1–7.

Kalinska E, Nartiss M. 2014. Pleistocene and Holocene aeolian sediments of different location and geological history: a new insight from rounding and frosting of quartz grains. *Quat Int* 328-329: 311–322. https://doi.org/10.1016/j.quaint.2013.08.038

Korschinek G, Bergmaier A, Faestermann T. 2010. A new value for the half-life of ^{10}Be by heavy-ion elastic recoil detection and liquid scintillation counting. *Nucl Instrum Methods Phys Res B* 268: 187–191.

Krijgsman W, Hilgen FJ, Raffi I, Sierro FJ, Wilson DS. 1999. Chronology, causes and progression of the Messinian salinity crisis. *Nature* 400: 652–655. https://doi.org/10.1038/23231

Lepage H, Masson M, Delanghe D, Le Bescond, C. 2019. Grain size analyzers: results of an intercomparison study. *SN Appl Sci* 1: 1100. https://doi.org/10.1007/s42452-019- 1133-9

Martinez M, Aguado R, Company M, Sandoval J, O'Dogherty L. 2020. Integrated astrochronology of the barremian stage (early cretaceous) and its biostratigraphic subdivisions. *Global Planet Change* 195: 103368. https://doi.org/10.1016/j.gloplacha.2020.103368

Merchel S, Herpers U. 1999. An update on radiochemical separation techniques for the determination of long-lived radionuclides *via* accelerator mass spectrometry. *Radiochim Acta* 84: 215–219.

Merchel S, Bremser W. 2004. First international 26Al interlaboratory comparison – Part I. *Nucl Instrum Methods Phys Res B* 223-224: 393–400.

Merchel S, Arnold M, Aumaître G, *et al.* 2008. Towards more precise ^{10}Be and 36Cl data from measurements at the 10(14 level: influence of sample preparation. *Nucl Instrum Methods Phys Res B* 266: 4921–4926

Miller KG, Browning JV, Schmelz WJ, Kopp RE, Mountain GS, Wright JD. 2020. Cenozoic sea-level and cryospheric evolution from deep-sea geochemical and continental margin records. *Sci Adv* 6: eaaz1346. https://doi.org/10.1126/sciadv.aaz1346

Nishiizumi K, Imamura M, Caffee MW, Southon JR, Finkel RC, McAninch J. 2007. Absolute calibration of 10Be AMS standards. *Nucl Instrum Methods Phys Res B* 258: 403–413. https://doi.org/10.1016/j.nimb.2007.01.297

Niedermann S. 2002. Cosmic-ray-produced noble gases in terrestrial rocks: dating tools for surface processes. *Rev Mineral Geochem* 47: 731–784. https://doi.org/10.2138/rmg.2002.47.16

Norris TL, Gancarz AJ, Rokop DJ, Thomas KW. 1983. Half-life of Al-26. *J Geophys Res* 88: 331–333.

Ogg JG. 2012. Geomagnetic polarity time scale. In: F.M. Gradstein, J. G. Ogg, M. Schmitz, G. Ogg (Eds.),*The Geologic Time Scale 2012*. Published by Elsevier B. V., pp. 85–113. https://doi. org/10. 1016/B978-0-444-59425–9.00005–6

Rabineau M, Leroux E, Daniel A, Bache F, Gorini C, Moulin M, *et al.* 2014. Quantifying subsidence and isostatic readjustment using sedimentary paleomarkers, example from the Gulf of Lion. *Earth Planet Sci Lett* 388: 353–366. https://doi.org/10.1016/j.epsl.2013.11.059

Rangin C., Le Pichon X., Hamon Y., Loget N., Crespy, A., 2010. Gravity tectonics in the SE Basin (Provence, France) imaged from seismic reflection data. *Bulletin de la Société Géologique de France* 181: 503–530. https://doi.org/10.2113/gssgfbull.181.6.503

Rixhon G, Braucher R, Bourlès D, Siame L, Bovy B, Demoulin A. 2011. Quaternary river incision in NE Ardennes (Belgium)-Insights from 10Be/26Al dating of river terraces. *Quat Geochronol* 6: 273–284. https://doi.org/10.1016/j.quageo.2010.11.001

Sartégou A, Bourlès DL, Blard P-H, *et al.* 2018. Deciphering landscape evolution with karstic networks: a Pyrenean case study. *Quat Geochronol* 43: 12–29.

Sartégou A, Blard P-H., Braucher R, *et al.* 2020. Late Cenozoic evolution of the Ariège River valley (Pyrenees) constrained by cosmogenic 26Al/10Be and 10Be/21Ne dating of cave sediments. *Geomorphology* 371: 107441. https://doi.org/10.1016/j.geomorph.2020.107441

Schwartz S, Gautheron C, Audin L, *et al.* 2017. Foreland exhumation controlled by crustal thickening in the Western Alps. *Geology* 45: 139–142. https://doi.org/10.1130/ G38561. 1

Sharifi A, Murphy LN, Pourmand A, *et al.* 2018. Early-Holocene greening of the Afro-Asian dust belt changed sources of mineral dust in West Asia. *Earth Planet Sci Lett* 481: 30–40. https://doi.org/10.1016/j.epsl.2017.10.001

Shuster DL, Farley KA. 2005. Diffusion kinetics of proton-induced ^{21}Ne, ^{3}He, and ^{4}He in quartz. *Geochim Cosmochim Acta* 69: 2349–2359. https://doi.org/10.1016/j.gca.2004.11.002

Vermeesch P, Balco G, Blard P-H, *et al.* 2012. Interlaboratory comparison of cosmogenic ^{21}Ne in quartz. *Quat Geochronol* 26: 20–28. doi:10.1016/j.quageo.2012.11.009

Zimmermann L, Avice G, Blard P-H., Marty B, Füri E, Burnard PG. 2018. Development of a new full-metal induction furnace for noble gas extraction. *Chem Geol* 480: 86–92.

Cite this article as: Demory F, Delanghe D, Braucher R, Blard P-H, Nutz A, Conesa G, Ségué-Passama G, Hollender F, Duvail C, Fioravanti A, Léanni L, Aster Team and Bellier O. 2024. Dating the late Miocene marine sediments around the southern middle Durance valley (Provence, SE France): new evidences for a Tortonian age *BSGF - Earth Sciences Bulletin* 195: 14.